

Lawrence Berkeley National Laboratory

LBL Publications

Title

Active-Source Seismic Imaging of Fault Re-Activation and Leakage: An Injection Experiment at the Mt Terri Rock Laboratory, Switzerland

Permalink

<https://escholarship.org/uc/item/5sc672nx>

Journal

Geophysical Research Letters, 50(23)

ISSN

0094-8276

Authors

Shadoan, Tanner A
Ajo-Franklin, Jonathan B
Guglielmi, Yves
[et al.](#)

Publication Date

2023-12-16

DOI

10.1029/2023gl104080

Copyright Information

This work is made available under the terms of a Creative Commons Attribution License, available at <https://creativecommons.org/licenses/by/4.0/>

Peer reviewed

Geophysical Research Letters[®]



RESEARCH LETTER

10.1029/2023GL104080

Key Points:

- measuring p-wave velocity changes during fault reactivation
- monitoring fault reactivation in an analog caprock for geologic carbon storage
- fracture damage zone modeling from p-wave velocities

Supporting Information:

Supporting Information may be found in the online version of this article.

Correspondence to:

J. B. Ajo-Franklin,
ja62@rice.edu

Citation:

Shadoan, T. A., Ajo-Franklin, J. B., Guglielmi, Y., Wood, T., Robertson, M., Cook, P., et al. (2023). Active-source seismic imaging of fault re-activation and leakage: An injection experiment at the Mt Terri Rock Laboratory, Switzerland. *Geophysical Research Letters*, 50, e2023GL104080. <https://doi.org/10.1029/2023GL104080>

Received 11 APR 2023

Accepted 10 NOV 2023

Author Contributions:

Conceptualization: Jonathan B.

Ajo-Franklin, Yves Guglielmi, Thomas M. Daley, Pierpaolo Marchesini, Jens Birkholzer

Data curation: Tanner A. Shadoan, Yves Guglielmi, Todd Wood, Michelle Robertson, Paul Cook, Chet Hopp, Verónica Rodríguez Tribaldos, Pierpaolo Marchesini

Formal analysis: Tanner A. Shadoan

Funding acquisition: Jonathan B.









Ajo-Franklin, Yves Guglielmi

Investigation: Tanner A. Shadoan, Todd Wood, Michelle Robertson, Paul Cook, Florian Soom, Chet Hopp, Verónica Rodríguez Tribaldos, Christophe Nussbaum

© 2023. The Authors.

This is an open access article under the terms of the [Creative Commons Attribution License](https://creativecommons.org/licenses/by/4.0/), which permits use, distribution and reproduction in any medium, provided the original work is properly cited.

Active-Source Seismic Imaging of Fault Re-Activation and Leakage: An Injection Experiment at the Mt Terri Rock Laboratory, Switzerland

Tanner A. Shadoan¹ , Jonathan B. Ajo-Franklin¹ , Yves Guglielmi² , Todd Wood², Michelle Robertson², Paul Cook², Florian Soom² , Thomas M. Daley² , Chet Hopp² , Verónica Rodríguez Tribaldos² , Pierpaolo Marchesini³ , Christophe Nussbaum⁴, and Jens Birkholzer²

¹Rice University, Houston, TX, USA, ²Lawrence Berkeley National Laboratory, Berkeley, CA, USA, ³Silixa Ltd, London, UK, ⁴Swisstopo, St-Ursanne, Switzerland

Abstract We conducted a time-lapse seismic experiment utilizing automated active seismic source and sensor arrays to monitor a reactivated fault within the Opalinus clay formation at the Mont Terri Rock Laboratory (Switzerland), an analog caprock for geologic carbon storage. A series of six brine injections were conducted into the so-called Main Fault to reactivate it. Seismic instrumentation in five monitoring boreholes on either side of the fault was used to continuously probe changes in P-wave travel-times associated with fault displacement and leakage. We performed time-lapse travel-time tomography on five hundred sequential data sets; this revealed a zone of decreased P-wave velocity, up to 16 m/s, during each injection cycle, followed by a velocity increase during shut-in. These results demonstrate varying elastic property perturbations, both spatially and temporally, along the fault plane during reactivation. We then interpreted these velocity changes in terms of fault dilation induced by pressurized fluids along the fault.

Plain Language Summary Faults within clay formation caprocks for CO₂ storage reservoirs are possible pathways for leakage and loss of containment. Understanding how these faults in clay-rich rocks reactivate and leak fluids is important for predicting, detecting, and preventing CO₂ movement. Passive seismic monitoring is challenging because of the lack of observable seismic events in such clay-rich fault rupture. In this study, we measure changes in P-wave velocity to monitor a fault reactivated by brine injections directly into the Main Fault at the Mont Terri Rock Laboratory, Switzerland. We use a recently developed time-lapse seismic technique called Continuous Active-Source Seismic Monitoring (CASSM), which allows us to make these measurements within a few minutes and observe small changes on the same timescale. We relate the measured changes in P-wave velocity to the opening of that fault damage zone by using a rock physics model, which helps explain changes in permeability within the fault zone.

1. Introduction

Faults and fractures are the main natural conduit for vertical fluid leakage from CO₂ reservoirs (Hill, 1996; Pruess, 2008; Ringrose et al., 2013; Vasco et al., 2018; Zhang et al., 2009). During injection, increased reservoir pore pressures can lead to fault reactivation and leakage (Vilarrasa, 2016; Vilarrasa et al., 2019), causing increased permeability due to the opening of cracks and fractures, thus allowing CO₂ to escape from the storage interval (Rutqvist, 2012; Vilarrasa et al., 2011; Yeo et al., 1998). A common practice for detecting these reactivated faults is to monitor for micro-seismic events passively; detecting these events gives insight into the location and mechanics of fault failure (B. P. Goertz-Allmann et al., 2014; B. Goertz-Allmann et al., 2017; Chen & Huang, 2020; Oye et al., 2022). However, this method is limited when monitoring reactivated faults in ductile clay-rich sealing units, where faults may fail primarily aseismically (i.e., Guglielmi et al., 2021) or the magnitude of the seismic events are below instrument sensitivity. These scenarios suggest that additional methods may be required for monitoring fault reactivation in sealing intervals with high clay content.

During fault reactivation, changes occur in both the rock frame and the pore fluid state, which can affect the modulus of the rock, which in turn can measurably change seismic velocities, V_p and V_s (Mavko et al., 2020). The opening of cracks and fractures induces a decrease in the asperity contact area, increasing normal and shear fracture compliance (Fortin et al., 2007; Pyrak-Nolte & Morris, 2000; Wenning et al., 2021). Time-lapse seismic

Methodology: Tanner A. Shadoan, Jonathan B. Ajo-Franklin, Yves Guglielmi, Michelle Robertson, Thomas M. Daley, Pierpaolo Marchesini
Project Administration: Jonathan B. Ajo-Franklin, Yves Guglielmi, Michelle Robertson
Resources: Yves Guglielmi, Todd Wood, Michelle Robertson, Paul Cook, Florian Soom, Christophe Nussbaum
Software: Tanner A. Shadoan, Jonathan B. Ajo-Franklin, Todd Wood, Paul Cook
Supervision: Jonathan B. Ajo-Franklin
Validation: Jonathan B. Ajo-Franklin, Yves Guglielmi, Chet Hopp, Verónica Rodríguez Tribaldos
Visualization: Yves Guglielmi
Writing – original draft: Tanner A. Shadoan, Jonathan B. Ajo-Franklin
Writing – review & editing: Tanner A. Shadoan, Jonathan B. Ajo-Franklin, Yves Guglielmi, Thomas M. Daley, Jens Birkholzer

approaches are increasingly important for monitoring subsurface changes, including variations in stress state (Herwanger et al., 2013) and fluid composition (Blazevic et al., 2020).

A time-lapse seismic approach was used by Rivet et al. (2016), who measured seismic velocity variations ($\Delta V_p/V_p$) from hammer shots up to 5% through a hydraulically stimulated fault in shale, which sheared aseismically. The velocity variations in their experiment were attributed to the pressurized pore fluids that forced fault permeability to increase (Rivet et al., 2016). To monitor changes in fault state during our experiment, we adopt a recently developed time-lapse seismic method, referred to as Continuous Active-Source Seismic Monitoring or CASSM (Ajo-Franklin et al., 2011; Daley et al., 2007; Silver et al., 2007). The CASSM method utilizes arrays of automated, semi-permanent seismic sources and receivers, arranged in a cross-well geometry, to tomographically measure small perturbations in seismic properties. The combination of permanence of the source-receiver geometry and automation allows for precise travel-time and attenuation measurements. In addition, the CASSM method provides complete data sets within a few minutes allowing for high temporal resolution monitoring of the subsurface. The CASSM method uses piezoelectric sources with high repeatability with precision on the order of 0.1 microseconds (Silver et al., 2007). Such precision allows for detecting minute changes expected during the opening of fractures and microcracks along faults. CASSM has been used to monitor changes in stress that have been a result of earthquake activity along a fault zone (Niu et al., 2008), fluid injection (Marchesini et al., 2017), and barometric pressure (Silver et al., 2007). In addition, CASSM successfully tracked a CO₂ plume in a saline aquifer (Daley et al., 2007, 2011) and induced fractures in a clay-rich formation (Ajo-Franklin et al., 2011). Alternatively, ambient noise tomography is a developing method that has successfully tracked changes in seismic velocity caused by earthquake activity along the San Andreas Fault (Breguier et al., 2008).

This paper will show that using P-wave tomographic imaging, the CASSM method was able to detect the spatial and temporal evolution of a reactivated fault patch in a clay-rich caprock analog at the Mont Terri rock laboratory, Switzerland. We demonstrate rapid response of the patch to injection pressure variations. In addition, we show that the observed changes in V_p can be explained by an increased fracture damage zone, with implications for longer-term fault healing and leakage.

2. Experimental Setting at the Mont Terri Rock Laboratory

The Mont Terri rock laboratory is situated on the south limb of the Mont Terri anticline within the Opalinus Clay formation, a geologic carbon storage caprock analog (Bossart et al., 2018). The Main Fault of Mont Terri is an approximately 3-m thick thrust fault, running through the Opalinus Clay and crossing the galleries of the Mont Terri rock laboratory (Jaeggi et al., 2018). To study fault processes, 23 boreholes penetrate or surround the fault for monitoring purposes (Figure 1a). The boreholes house permanently installed instruments including optical fibers for distributed acoustic (DAS), strain (DSS) and temperature (DTS) sensing (Hopp et al., 2022), pressure sensors, tiltmeters, fault displacement sensors, and passive acoustic/seismic sensors. In this paper, we primarily focus on the CASSM data.

The CASSM system is located in five boreholes on either side of the fault (Figure 1a). Three boreholes have 8 piezoelectric seismic sources apiece (24 total); the other two have arrays of 22 hydrophones apiece (44 total). The receiver boreholes (BFS-B3 and BFS-B4) are in the footwall of the fault, while the source boreholes (BFS-B5, BFS-B6, and BFS-B7) are in the hanging-wall. Unfortunately, however, two sources stopped working before the injection experiment. Both the sources and receivers are fluid coupled. During automated CASSM acquisition, each source was shot and stacked 16 times to increase signal-to-noise ratio (SNR) before cycling to the next source. The seismic data were recorded at 48,000 samples/sec with a 100 ms record length for each shot. Spectral analysis shows that the central frequency of the recorded P-wave first arrival pulse is 1.4 kHz. An epoch, which includes all 24 sources, took approximately 8 min to complete, defining the temporal resolution between complete data sets.

We use this CASSM system to monitor the hydro-mechanical reactivation of a portion of the Main Fault. The experiment occurred on 21 November 2020, when brine was injected directly into the upper 2.4 m of the fault zone at 476.2 m depth (BFS-B2 in Figure 1a). Throughout ~8 hr, we injected six times at constant flow rates for 10 min, except for the last injection, which was 20 min (Figure 1b). The injection interval was shut-in between injection periods. The flow rate values were selected from previous hydromechanical test results done in another area of the fault (Guglielmi et al., 2020). The idea was to keep flow rates low enough to avoid any influence of the flow rate on fault activation, but large enough to generate a seismically visible flow path development. The first two injections had lower flow rates, around 2 and 6 L/min, respectively, compared to the last four, around

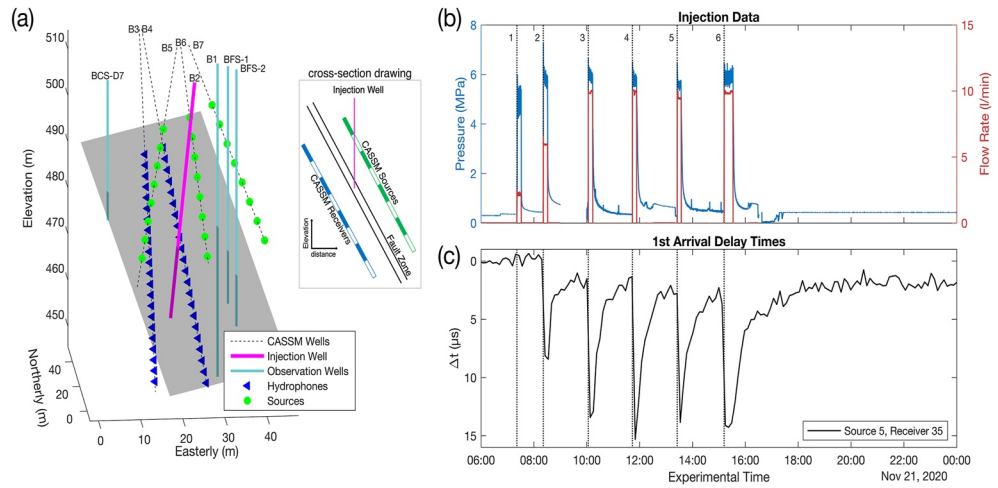


Figure 1. (a) 3D map showing key boreholes, CASSM sources and receivers, and the fault plane for images in Figure 2, Figures 4c–4d, and Figure S4 in Supporting Information S1. Borehole BFS-B1 through BFS-B7 are labeled as B1 through B7. The inset represents a cross-section drawing of the fault with relative position of the CASSM sources and receivers. (b) Injection pressures and flow rates during the six brine injections. (c) An example delay-time curve for a single source-receiver pair, with vertical lines representing the beginning of the six injections.

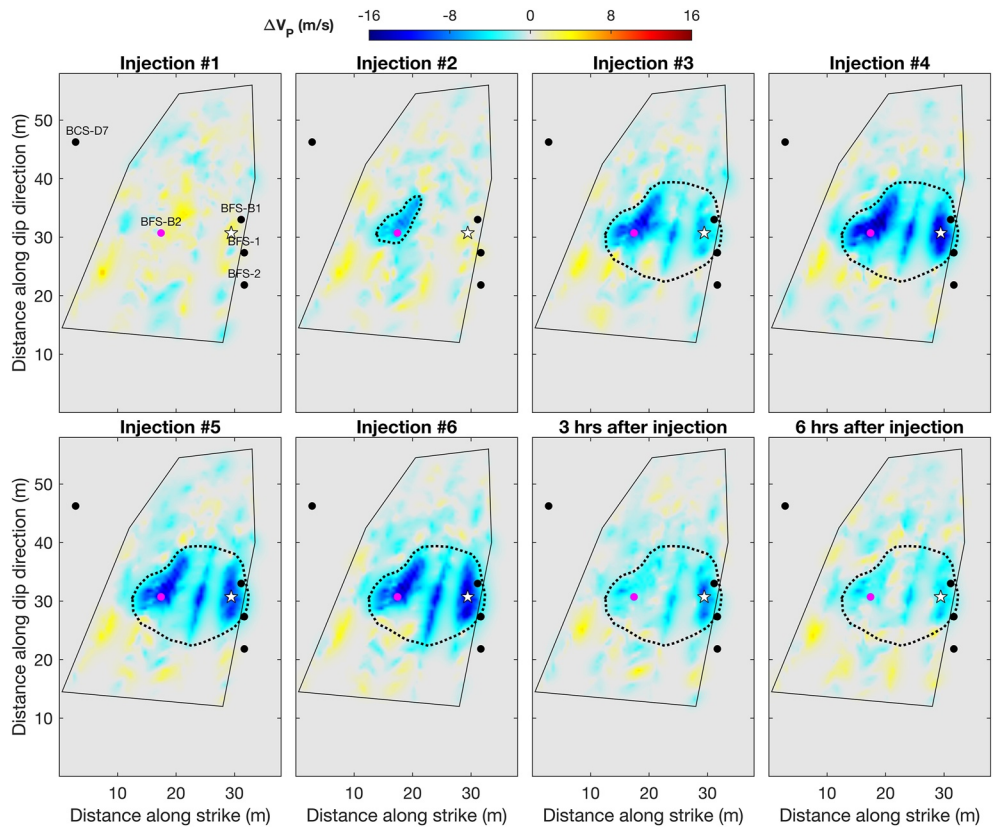


Figure 2. Time-lapse travel-time tomography results for all six injection cycles as well as at three and six hours after the last injection. Each panel represents a slice through the 3D volume and parallel to the so-called Main Fault at the Mont Terri (orientation of the slice represented in 3D in Figure 1a). The solid black box represents CASSM’s imaging extent. The dotted black area represents our interpretation of the damage zone along the fault. Key boreholes which intersect the fault are plotted on the images, including the injection borehole, BFS-B2 (magenta). The white star is ~ 12 m easterly along fault strike from the injection borehole and represents the location of the second ΔV_p curve (red) in Figure 3.

10 L/min. When injection pressures reached between 5 and 6 MPa, the fault reactivated, which is in accordance with the local stress state (Guglielmi et al., 2020). During the third injection cycle, at which point ~178 L had been injected, a hydraulic connection was created with boreholes intersecting the fault 15–18 m along strike from the injection point, including BFS-B1, BFS-1, and BFS-2 (Figure 1a). Interestingly, no hydraulic connection was observed at BCS-D7, which is at a similar distance from the injection borehole as BFS-B1. During the ~8 hr injection sequence, the system recorded 64 epochs or CASSM cycles, where each cycle takes ~8 min, including at least two epochs during each injection and shut-in period.

3. 3D Time-Lapse Travel-Time Tomography

In this study, our primary focus was on direct P-wave arrival analysis. Both tube-wave to P-wave and P-wave to tube-wave mode conversions are also observable in the source gathers (Figure S1a in Supporting Information S1). Unfortunately, no shear wave information was recovered due to the water coupling of the sources and receivers in the boreholes.

We compute 3D time-lapse travel-time tomography to image the changes in P-wave velocity (ΔV_p) along the fault during the brine injections. Four main components were used to compute the tomography:

1. Delay-time data (Δt) of the first arrivals for all source and receiver pairs were computed for all epochs between 6:00 a.m. to the end of the day, 21 November 2020 (i.e., Figure 1c). To compute the delay times, we followed the methodology of Silver et al. (2007) to get sub-sample delay times of the first arrivals (Shadoan et al., 2021). This includes converting source gathers (figure S1a in Supporting Information S1) to temporal gathers (figure S1b in Supporting Information S1) and creating a 30 ms window with 3 ms tapers around the first arrival. We then interpolate the waveform 10,000 times the sampling rate to get sub-sample delay times and cross-correlate all epochs to the legacy epoch, the last full epoch before the first injection. We apply this same workflow to the ten days leading up to the injections to show CASSM's background stability; for example, source-receiver pair 5–35 has a delay time standard deviation of 0.73 microseconds (figure S2 in Supporting Information S1). For the time-lapse travel-time tomography, we removed 15% of the source-receiver pairs with the highest standard deviation, which correspond to pairs with long offsets and low SNR. Observations show that delay times during injections reached up to 16 μ s (Figure 1c), which is greater than the 1 μ s delay time background noise levels (figure S2 in Supporting Information S1).
2. A 3D absolute-velocity (V_p) background model was then generated from hand-picked first arrivals of the legacy epoch (figure S3 in Supporting Information S1). The average background V_p within the fault zone is approximately 3,280 m/s. This model was used as the baseline for the time-lapse tomography calculations and to generate accurate ray path geometries.
3. The accurate ray-path geometries were generated using an unstructured grid eikonal solver with reverse ray-tracing (TTCR, Giroux, 2021).
4. Lastly, we exploit a spatially variable regularization term (P) to help constrain the ΔV_p in our linear travel-time tomography to within the ~3-m wide fault zone. This term is needed, due to the lack of ray-paths traveling parallel to the fault zone and is a prior assumption.

We invert for changes in P-wave slowness for every epoch such that

$$\Delta s = \begin{bmatrix} G \\ \lambda_1 D \\ \lambda_2 P \end{bmatrix} \begin{bmatrix} \Delta t \\ 0 \\ 0 \end{bmatrix}, \quad (1)$$

where

$$P = \begin{bmatrix} \Omega(x) & & & & \\ & \Omega(x) & & & \\ & & \ddots & & \\ & & & \Omega(x) & \\ & & & & \Omega(x) \end{bmatrix}, \quad (2)$$

and

$$\Omega(x) = \begin{cases} 0, & \text{if } x \text{ is inside fault} \\ 1, & \text{if } x \text{ is outside fault} \\ 0.5, & \text{if } x \text{ is in transition zone,} \end{cases} \quad (3)$$

Δs is the change in slowness, Δt are the differential delay times, G is the tomographic kernel, D is a first order difference operator, P is the spatially variable regularization term, λ_1 and λ_2 are the regularization parameters for D and P , respectively, and x is the physical location of the model cell; where each model cell is a cube of 0.5 m edges. Δs is then converted to ΔV_p by comparing it to the background model. This computation was done for all epochs before, during, and after the injections.

4. ΔV_p Model of the Injection Cycles

Eight ΔV_p images are shown in Figure 2, six of these correspond in time to the middle of each injection cycle, while the last two images represent three and six hours after the last injection. During the first injection, no clear ΔV_p anomalies were detected, since values range between ± 2 m/s, which is similar to the pre-stimulation range. During the second injection, there is an asymmetric 32.3 m^2 area of negative ΔV_p (approximately -5 to -10 m/s) immediately around the injection borehole. The third injection ΔV_p image shows a larger anomaly near the injection well with two smaller patches north-easterly along the fault for a total of three patches. ΔV_p values within the anomaly range between -5 and -14 m/s. ΔV_p images for injection cycles 4 through 6 appear to show the same three streaks, but with a greater negative ΔV_p to -16 m/s, which is a 0.5% decrease in V_p . After the last injection, such as three and six hours after the last injection (Figure 2), V_p values begin to recover toward pre-injection values.

We ran a series of forward modeling checkerboard tests with different-sized checkerboards to investigate the three streaks observed in the ΔV_p images (figures S4a and S4b in Supporting Information S1). The three streaks are also observed in the checkerboard tests (i.e., Inoue et al., 1990; Zelt & Barton, 1998). This suggests that these three streaks represent areas of high seismic coverage separated by areas of low seismic coverage along the fault zone, which is a product of the CASSM source and receiver geometry, rather than a geologic process. From these tests, we also observe the outer imaging limits (solid outline, Figure S4 in Supporting Information S1 and Figure 2). With this, we interpret the three streaks in the ΔV_p images for the third through sixth injection cycles as a single patch that is 248.7 m^2 , which is the dotted closure drawn in those images (Figure 2). Following this interpretation, we ran the forward model with the single patch case. The results show the three streaks, confirming that these features are not geologic.

Figure 3 shows ΔV_p time series for two locations along the ΔV_p images, the first is at the injection borehole (BFS-B2) and the second location is ~ 12 m easterly along strike (i.e., magenta circle and white star, respectively, in Figure 2). Five significant negative ΔV_p events at the injection borehole correspond to the last five injection cycles. Beginning at the second injection through the fourth injection cycle, P-wave velocity perturbations were increasingly negative before remaining constant through the fifth and sixth injections. At the second location, only the last four injection cycles were captured, but with a large negative ΔV_p change compared to the change at the injection borehole. The maximum negative ΔV_p values are approximately 8 and 16 m/s at the injection well and the second location, respectively. During the shut-in periods, ΔV_p would partially recover back to background levels before the next injection cycle. After the last injection cycle, the curves appear to plateau to different ΔV_p background levels at -2 and -5 m/s for the first and second locations, respectively.

5. Fracture Damage Zone Modeling

The maximum P-wave velocity perturbations ($\Delta V_p/V_p$) are approximately 0.5%, which is less than that of Rivet et al. (2016), who measured velocity perturbations of a similar fault reactivation experiment. We interpret negative ΔV_p to represent the areas of the fault that have been reactivated. The changes in seismic velocity are due to variations in pore pressure during injection and the opening and shear of fractures within the fault zone. During the first injection, with no significant negative ΔV_p anomalies, the small 21-L injection volume and the

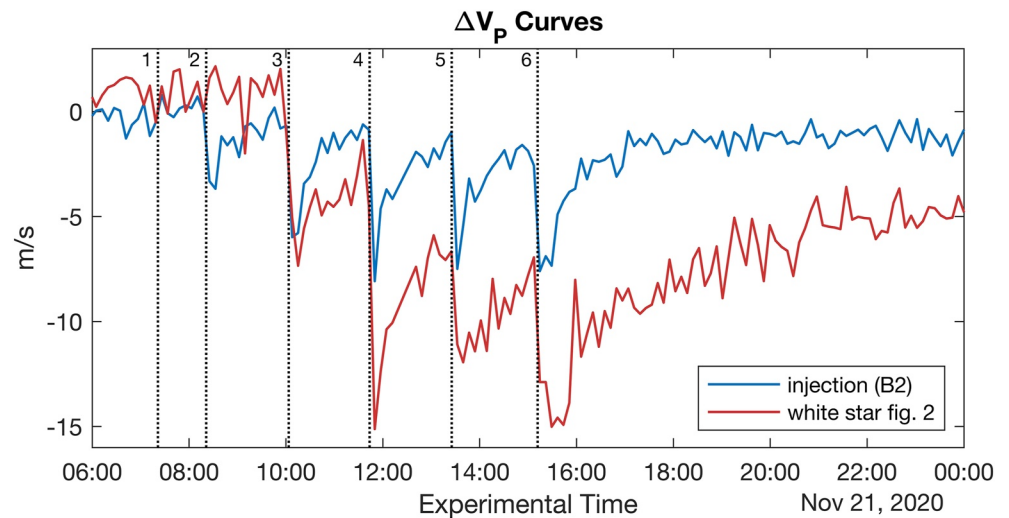


Figure 3. ΔV_p versus calendar time for two locations along the ΔV_p images. The blue curve is located at the injection borehole and the red curve is located at the white star in Figure 2, which is ~ 12 m easterly along strike. Vertical dotted lines represent the beginning of each injection cycle (i.e., same time as in Figures 1b and 1c).

relatively low injection pressure of 5.3 MPa (below the estimated fault reactivation pressure from Guglielmi et al., 2020) limited fault reactivation and leakage to near the injection borehole. This result corresponds with Guglielmi et al. (2020), who suggested that 5.43 MPa of injection pressure is required to reactivate the fault hydro-mechanically. The P-wave velocity anomaly appears in the second cycle while injection pressure reaches 5.8 MPa and injection volume reaches 76 L (Figure 1b). The asymmetric behavior of the negative ΔV_p patches in the ΔV_p images, coupled with the fact that hydraulic connection was established with BFS-B1 but not with BCS-D7, suggests that there is a preferred direction of fault reactivation and fault leakage, which is primarily in direction of fault strike or northeasterly. Many hours after the last injection cycle, ΔV_p values remain elevated above background levels (Figure 3), suggesting permanent or long-term damage.

During each injection cycle, pore pressure is the dominant driver of velocity perturbations, but the residual velocity change indicates damage. CT scans of the Main Fault drill-core from the BFS-B1 well (EPFL, 2021) show planar voids (blue) that represent thin open cracks and worm burrows (yellow) in the intact rock core (Figure 4a). In the principal shear zone, these worm burrows appear granular compared to the thin pencil-like burrows observed elsewhere, suggesting they were pulverized by fault shear. We hypothesize that during the stimulation, multiple of these fractures are opened within the 3-m fault zone. Therefore these fractures are the primary pathway for fluid flow and fault leakage along the fault zone.

We model the opening of these fractures, by relating both ΔV_p and effective stress to the cumulative aperture of all fractures across the 3-m fault zone (figure S5 in Supporting Information S1). We refer to this cumulative fracture aperture as the damage zone thickness. The effective stress is computed by subtracting the injection pressures from the estimated lithostatic pressures at the fault zone of 7.3 MPa from Guglielmi et al. (2020). Our damage zone thickness model is explained in detail in Supporting Information S1; we provide a conceptual explanation here. Our model assumes that, as the fractures are opened during injection, they are filled with a granular pack of the same material as the host matrix (schematic drawing in Figure 4b). Therefore, fracture compliance is controlled by this granular packing and the pore fluid inside the fracture. Using the Walton Smooth contact theory model (Walton, 1987), we computed the elastic properties of the granular material inside the fracture, where the bulk and shear modulus are a function of effective stress on the fracture. In our case, effective stress varies with time along the fault during each injection cycle. In our current model, we estimate the elastic properties of the host material by using the average V_p from our background model (figure S4 in Supporting Information S1) as well as additional information from laboratory tests done on samples from the same fault zone (Wenning et al., 2021), such as an appropriate V_p/V_s ratio and density values. We then calculated the elastic properties of this material in the case where the pores are filled with the injection fluid using Gassmann's fluid substitution (Gassmann, 1951). We then calculate the normal and shear compliance of the fracture using the

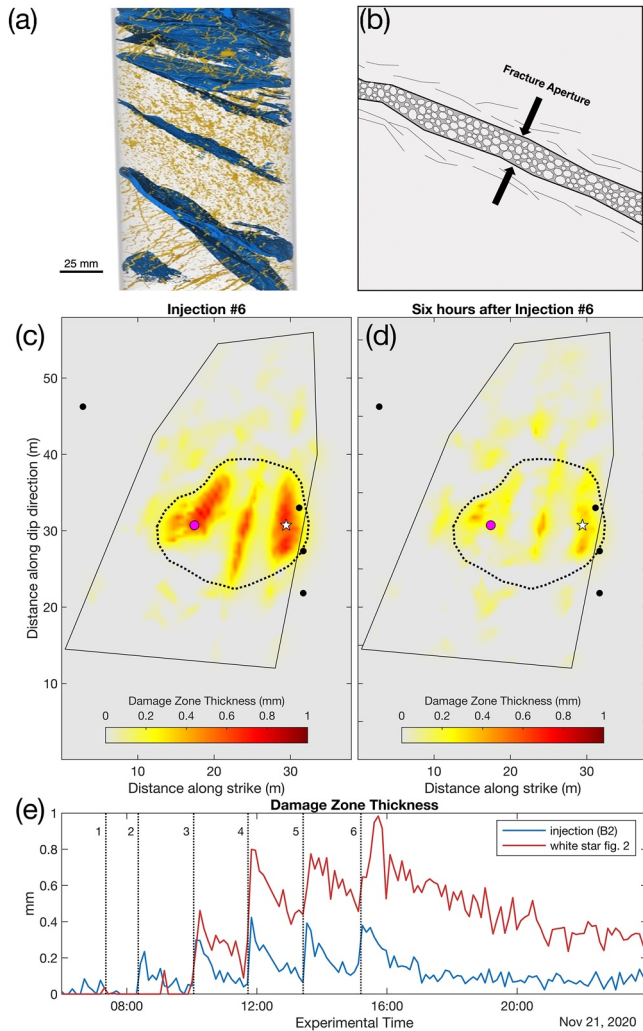


Figure 4. (a) A CT scan of a core from BFS-B1 of the Main fault at the Mont Terri rock laboratory, where blue represent thin cracks and yellows represent worm burrows (EPFL, 2021). The granular texture of the burrows between the cracks represent pulverized grains due to fault shear. (b) A schematic drawing of our fracture damage zone model. Panels (c) and (d) are damage zone thickness images during the sixth injection cycle and then six hours after, respectively. (e) Damage zone thickness curves for the same locations explained in Figure 3.

utilized a rock-physics model based on contact theory to interpret the ΔV_p in terms of stress state and damage zone thickness. During injection, we estimate that the damage zone along the fault reaches a cumulative ~ 1 mm thickness, suggesting increased permeability. After shut-in, damage zone thickness values partially recover, with the residual aperture suggesting long-term damage along the fault. This study suggests the existence of a seismic signature for residual permeability after reactivation, a promising target for future monitoring approaches.

Data Availability Statement

Data, including the CASSM source and receiver geometry, first arrival picks, P-wave arrival delay times for all source-receiver pairs, injection flow rate/pressure, and the time-lapse travel-time tomography matrices, can be found in the following OSF repository: <https://osf.io/d6b2a> (Shadoan, 2023).

Backus (1962) average (Mavko et al., 2020). After the fracture compliance is estimated, the method of Coates and Schoenberg (1995) is used to calculate the anisotropic elastic perturbation induced by the fault damage zone. Since our experiment has insufficient angular coverage to conduct anisotropic tomography, the resulting group velocity curves are averaged over the sampled angular domain to estimate an isotropic velocity perturbation generated by the fracture.

Our approach generally predicts that damage zone thickness is proportional to negative ΔV_p values with an overprint of the effective stress state (figure S5 in Supporting Information S1). While not directly calculated in this paper, permeability would increase during periods of elevated damage zone thickness because increased fracture aperture would directly impact fluid movement within the fault zone. The predicted damage zone thickness variation values peak at 1 mm during the sixth injection cycle (Figure 4c). Conversely, the damage zone thickness variation values are near zero in areas outside of the fault reactivation zone, suggesting little to no fault dilation. After fault reactivation, such as six hours after the last injection cycle, damage zone thickness values are still elevated to around 0.4 mm (Figure 4d). Furthermore, from looking at damage zone thickness values versus calendar time, they appear to plateau at a new background level of around 0.1–0.3 mm depending on the location within the patch (Figure 4e). This suggests long-term fault damage, which has important implications for fault sealing, fluid loss, and longer-term healing processes during geologic carbon storage operations. We should note that these damage thickness estimates should be viewed as cumulative and do not necessarily represent a single discrete zone of alteration; this distinction, while not affecting the change in volumetric compliance, might impact inferred permeability changes.

6. Conclusion

We utilized the Continuous Active-Source Seismic Monitoring (CASSM) method to observe the seismic signature of hydro-mechanical fault reactivation during an experiment at the Mont Terri Rock Laboratory. CASSM data was collected continuously before, during, and after fluid injections to monitor the spatio-temporal elastic property variations within the reactivated fault patch. We performed time-lapse travel-time tomography to quantify ΔV_p evolution in space and time. Along the fault plane, we observed a negative ΔV_p anomaly (up to -16 m/s), asymmetrically extending from the injection well, that grew in size primarily northeasterly along strike. This observation suggested a preferred direction of fault reactivation and patch growth. We

Acknowledgments

The authors are grateful to the partners of the Mont Terri Project that contributed to the funding of the FS-B experiment: the Swiss Federal Office of Topography (Swisstopo), the Swiss Federal Nuclear Safety Inspectorate (ENSI), the Japanese 689 Atomic Energy Agency (JAEA), the Institute of Radioprotection and of Nuclear Safety 690 (IRSN, France), TOTAL SE, CHEVRON, SHELL, the Federal Institute for Geosciences and Natural Resources (BGR, Hannover), and the U.S. Department of Energy. The Mont Terri Project is an international research project for the hydrogeological, geochemical, and geotechnical characterizations of a clay formation (Opalinus Clay). Funding for the FS-B CASSM deployment and data described in this study was provided by the Assistant Secretary for Fossil Energy as part of the Carbon Storage program of the U.S. Department of Energy under contract FP00007630. Additional analysis support was provided by the U.S. Department of Energy, Office of Fossil Energy and Carbon Management (DOE FECM) under contract DE-FE00032058.

References

Ajo-Franklin, J., Daley, T., Butler-Veytia, B., Peterson, J., Wu, Y., Kelly, B., & Hubbard, S. (2011). Multi-level continuous active source seismic monitoring (ML-CASSM): Mapping shallow hydrofracture evolution at a TCE contaminated site. In *2011 SEG annual meeting*.

Backus, G. E. (1962). Long-wave elastic anisotropy produced by horizontal layering. *Journal of Geophysical Research*, *67*(11), 4427–4440. <https://doi.org/10.1029/jz067i011p04427>

Blazevic, L. A., Bodet, L., Pasquet, S., Linde, N., Jougnot, D., & Longuevergne, L. (2020). Time-lapse seismic and electrical monitoring of the vadose zone during a controlled infiltration experiment at the plomeur hydrological observatory, France. *Water*, *12*(5), 1230. <https://doi.org/10.3390/w12051230>

Bossart, P., Bernier, F., Birkholzer, J., Bruggeman, C., Connolly, P., Dewonck, S., et al. (2018). *Mont Terri rock laboratory, 20 years of research: Introduction, site characteristics and overview of experiments* (pp. 3–22). Mont Terri rock laboratory.

Brenguier, F., Campillo, M., Hadziioannou, C., Shapiro, N. M., Nadeau, R. M., & Larose, E. (2008). Postseismic relaxation along the San Andreas at Parkfield from continuous seismological observations. *Science*, *321*(5895), 1478–1481. <https://doi.org/10.1126/science.1160943>

Chen, T., & Huang, L. (2020). Optimal design of microseismic monitoring network: Synthetic study for the kimberlina CO₂ storage demonstration site. *International Journal of Greenhouse Gas Control*, *95*, 102981. <https://doi.org/10.1016/j.ijggc.2020.102981>

Coates, R. T., & Schoenberg, M. (1995). Finite-difference modeling of faults and fractures. *Geophysics*, *60*(5), 1514–1526. <https://doi.org/10.1190/1.1443884>

Daley, T. M., Ajo-Franklin, J. B., & Doughty, C. (2011). Constraining the reservoir model of an injected CO₂ plume with crosswell CASSM at the Frio-II brine pilot. *International Journal of Greenhouse Gas Control*, *5*(4), 1022–1030. <https://doi.org/10.1016/j.ijggc.2011.03.002>

Daley, T. M., Solbau, R. D., Ajo-Franklin, J. B., & Benson, S. M. (2007). Continuous active-source seismic monitoring of CO₂ injection in a brine aquifer. *Geophysics*, *72*(5), A57–A61. <https://doi.org/10.1190/1.2754716>

EPFL. (2021). Study report fs-b experiment high-resolution micro-ct measurements on drillcores of the main fault small-scale geological characterization of fault zone in shale Mont-Terri consortium. Project fsb8-ph24.

Fortin, J., Guéguen, Y., & Schubnel, A. (2007). Effects of pore collapse and grain crushing on ultrasonic velocities and Vp/Vs. *Journal of Geophysical Research*, *112*(B8), B08207. <https://doi.org/10.1029/2005jb004005>

Gassmann, F. (1951). Elastic waves through a packing of spheres. *Geophysics*, *16*(4), 673–685. <https://doi.org/10.1190/1.1437718>

Giroux, B. (2021). TCRPY: A python package for traveltimes computation and raytracing. *SoftwareX*, *16*, 100834. <https://doi.org/10.1016/j.softx.2021.100834>

Goertz-Allmann, B., Gibbons, S., Oye, V., Bauer, R., & Will, R. (2017). Characterization of induced seismicity patterns derived from internal structure in event clusters. *Journal of Geophysical Research: Solid Earth*, *122*(5), 3875–3894. <https://doi.org/10.1002/2016jb013731>

Goertz-Allmann, B. P., Kühn, D., Oye, V., Bohloli, B., & Aker, E. (2014). Combining microseismic and geomechanical observations to interpret storage integrity at the in Salah CCS site. *Geophysical Journal International*, *198*(1), 447–461. <https://doi.org/10.1093/gji/ggu010>

Guglielmi, Y., Nussbaum, C., Cappa, F., De Barros, L., Rutqvist, J., & Birkholzer, J. (2021). Field-scale fault reactivation experiments by fluid injection highlight aseismic leakage in caprock analogs: Implications for CO₂ sequestration. *International Journal of Greenhouse Gas Control*, *111*, 103471. <https://doi.org/10.1016/j.ijggc.2021.103471>

Guglielmi, Y., Nussbaum, C., Rutqvist, J., Cappa, F., Jeanne, P., & Birkholzer, J. (2020). Estimating perturbed stress from 3D borehole displacements induced by fluid injection in fractured or faulted shales. *Geophysical Journal International*, *221*(3), 1684–1695. <https://doi.org/10.1093/gji/ggaa103>

Herwanger, J. V., Mohamed, F. R., Newman, R., & Vejbæk, O. (2013). Time-lapse seismic data-calibrated geomechanical model reveals hydraulic fracture re-orientation. In *2013 SEG annual meeting*.

Hill, D. P. (1996). Earthquakes and carbon dioxide beneath mammoth mountain, California. *Seismological Research Letters*, *67*(1), 8–15. <https://doi.org/10.1785/gssrl.67.1.8>

Hopp, C., Guglielmi, Y., Rinaldi, A. P., Soom, F., Wenning, Q., Cook, P., et al. (2022). The effect of fault architecture on slip behavior in shale revealed by distributed fiber optic strain sensing. *Journal of Geophysical Research: Solid Earth*, *127*(1), e2021JB022432. <https://doi.org/10.1029/2021jb022432>

Inoue, H., Fukao, Y., Tanabe, K., & Ogata, Y. (1990). Whole mantle p-wave travel time tomography. *Physics of the Earth and Planetary Interiors*, *59*(4), 294–328. [https://doi.org/10.1016/0031-9201\(90\)90236-q](https://doi.org/10.1016/0031-9201(90)90236-q)

Jaeggi, D., Laurich, B., Nussbaum, C., Schuster, K., & Connolly, P. (2018). Tectonic structure of the “main fault” in the Opalinus clay, Mont Terri rock laboratory (Switzerland). In *Mont Terri rock laboratory, 20 years* (pp. 69–86). Springer.

Marchesini, P., Ajo-Franklin, J. B., & Daley, T. M. (2017). In situ measurement of velocity-stress sensitivity using crosswell continuous active-source seismic monitoring in situ velocity-stress sensitivity. *Geophysics*, *82*(5), D319–D326. <https://doi.org/10.1190/geo2017-0106.1>

Mavko, G., Mukerji, T., & Dvorkin, J. (2020). *The rock physics handbook*. Cambridge university press.

Niu, F., Silver, P. G., Daley, T. M., Cheng, X., & Majer, E. L. (2008). Preseismic velocity changes observed from active source monitoring at the Parkfield Safod drill site. *Nature*, *454*(7201), 204–208. <https://doi.org/10.1038/nature07111>

Oye, V., Stanchits, S., Babarinde, O., Bauer, R., Dichiarante, A. M., Langet, N., & Frailley, S. (2022). Cubic-meter scale laboratory fault re-activation experiments to improve the understanding of induced seismicity risks. *Scientific Reports*, *12*(1), 8015. <https://doi.org/10.1038/s41598-022-11715-6>

Pruess, K. (2008). Leakage of CO₂ from geologic storage: Role of secondary accumulation at shallow depth. *International Journal of Greenhouse Gas Control*, *2*(1), 37–46. [https://doi.org/10.1016/s1750-5836\(07\)00095-3](https://doi.org/10.1016/s1750-5836(07)00095-3)

Pyrak-Nolte, L., & Morris, J. (2000). Single fractures under normal stress: The relation between fracture specific stiffness and fluid flow. *International Journal of Rock Mechanics and Mining Sciences*, *37*(1–2), 245–262. [https://doi.org/10.1016/s1365-1609\(99\)00104-5](https://doi.org/10.1016/s1365-1609(99)00104-5)

Ringrose, P., Mathieson, A., Wright, I., Selama, F., Hansen, O., Bissell, R., et al. (2013). The in Salah CO₂ storage project: Lessons learned and knowledge transfer. *Energy Procedia*, *37*, 6226–6236. <https://doi.org/10.1016/j.egypro.2013.06.551>

Rivet, D., De Barros, L., Guglielmi, Y., Cappa, F., Castilla, R., & Henry, P. (2016). Seismic velocity changes associated with aseismic deformations of a fault stimulated by fluid injection. *Geophysical Research Letters*, *43*(18), 9563–9572. <https://doi.org/10.1002/2016gl070410>

Rutqvist, J. (2012). Fractured rock stress–permeability relationships from in situ data and effects of temperature and chemical–mechanical couplings. *Crustal Permeability*, 65–82. <https://doi.org/10.1002/9781119166573.ch8>

Shadoan, T. (2023). Continuous active-source seismic monitoring of a fault reactivation experiment (FS-B) at Mt Terri rock laboratory (Switzerland) [Dataset]. OSF. <https://doi.org/10.17605/OSF.IO/D6B2A>

Shadoan, T., Ajo-Franklin, J., Guglielmi, Y., Wood, T., Robertson, M., Cook, P., et al. (2021). Continuous active-source seismic monitoring of brine injections directly in the main fault at Mont Terri, Switzerland. In *SEG/AAPG/SEPM first international meeting for applied geoscience & energy*.

- Silver, P. G., Daley, T. M., Niu, F., & Majer, E. L. (2007). Active source monitoring of cross-well seismic travel time for stress-induced changes. *Bulletin of the Seismological Society of America*, 97(1B), 281–293. <https://doi.org/10.1785/0120060120>
- Vasco, D. W., Bissell, R. C., Bohloli, B., Daley, T. M., Ferretti, A., Foxall, W., et al. (2018). Monitoring and modeling caprock integrity at the in Salah carbon dioxide storage site, Algeria. *Geological carbon storage: Subsurface seals and caprock integrity*, 243–269.
- Vilarrasa, V. (2016). The role of the stress regime on microseismicity induced by overpressure and cooling in geologic carbon storage. *Geofluids*, 16(5), 941–953. <https://doi.org/10.1111/gfl.12197>
- Vilarrasa, V., Carrera, J., Olivella, S., Rutqvist, J., & Laloui, L. (2019). Induced seismicity in geologic carbon storage. *Solid Earth*, 10(3), 871–892. <https://doi.org/10.5194/se-10-871-2019>
- Vilarrasa, V., Koyama, T., Neretnieks, I., & Jing, L. (2011). Shear-induced flow channels in a single rock fracture and their effect on solute transport. *Transport in Porous Media*, 87(2), 503–523. <https://doi.org/10.1007/s11242-010-9698-1>
- Walton, K. (1987). The effective elastic moduli of a random packing of spheres. *Journal of the Mechanics and Physics of Solids*, 35(2), 213–226. [https://doi.org/10.1016/0022-5096\(87\)90036-6](https://doi.org/10.1016/0022-5096(87)90036-6)
- Wenning, Q. C., Madonna, C., Zappone, A., Grab, M., Rinaldi, A. P., Plötze, M., et al. (2021). Shale fault zone structure and stress dependent anisotropic permeability and seismic velocity properties (Opalinus Clay, Switzerland). *Journal of Structural Geology*, 144, 104273. <https://doi.org/10.1016/j.jsg.2020.104273>
- Yeo, I., De Freitas, M., & Zimmerman, R. (1998). Effect of shear displacement on the aperture and permeability of a rock fracture. *International Journal of Rock Mechanics and Mining Sciences*, 35(8), 1051–1070. [https://doi.org/10.1016/s0148-9062\(98\)00165-x](https://doi.org/10.1016/s0148-9062(98)00165-x)
- Zelt, C. A., & Barton, P. J. (1998). Three-dimensional seismic refraction tomography: A comparison of two methods applied to data from the Faeroe basin. *Journal of Geophysical Research*, 103(B4), 7187–7210. <https://doi.org/10.1029/97jb03536>
- Zhang, Y., Oldenburg, C. M., Finsterle, S., Jordan, P., & Zhang, K. (2009). Probability estimation of CO₂ leakage through faults at geologic carbon sequestration sites. *Energy Procedia*, 1(1), 41–46. <https://doi.org/10.1016/j.egypro.2009.01.008>